Orbital Hall effect and topology on a two-dimensional triangular lattice: From bulk to edge

Anderson L. R. Barbosa [1,*] Luis M. Canonico [2] Jose H. García,[2] and Tatiana G. Rappoport [3,4,†]

[1]*Departamento de Física, Universidade Federal Rural de Pernambuco, 52171-900 Recife, Pernambuco, Brazil*
[2]*Catalan Institute of Nanoscience and Nanotechnology (ICN2), CSIC and BIST, Campus UAB, Bellaterra, 08193 Barcelona, Spain*
[3]*Centro de Física das Universidade do Minho e do Porto and Departamento de Física, Universidade do Minho, 4710-057 Braga, Portugal*
[4]*Instituto de Física, Universidade Federal do Rio de Janeiro, C.P. 68528, 21941-972 Rio de Janeiro, Rio de Janeiro, Brazil*

We investigate a generalized multiorbital tight-binding model on a triangular lattice, a system prevalent in a wide range of two-dimensional materials and particularly relevant for simulating transition metal dichalcogenide monolayers. We show that the interplay between spin-orbit coupling and different symmetry-breaking mechanisms leads to the emergence of four distinct topological phases [Eck *et al.*, Phys. Rev. B **107**, 115130 (2023)]. Remarkably, this interplay also triggers the orbital Hall effect with distinguished characteristics. Furthermore, by employing the Landauer-Büttiker formula, we establish that in the orbital Hall insulating phase, the orbital angular momentum is carried by edge states present in nanoribbons with specific terminations. We also show that they do not have the same topological protection against the disorder of the edge states as a first-order topological insulator.

I. INTRODUCTION

The past few decades have seen growing interest in manipulating the quantum degrees of freedom for developing new quantum devices. The emergence of two-dimensional materials and the tunability of their properties added to their capability to sustain highly crystalline interfaces reignited the excitement in spintronics and provided a platform for tackling long-standing challenges in the field while paving the way for groundbreaking technological applications like spin-orbit-based memory systems and ultracompact devices [1–3]. The tunability of the properties of the two-dimensional (2D) materials also enabled the control of the spin-orbit coupling, which is essential for electrical manipulation of the spins. Nonetheless, due to its electrostatic origin, this interaction tends to appear in heavy metals, which are scarce, and their usage poses environmental risks.

Recently, researchers have turned their attention to the manipulation of the orbital degrees of freedom and exploiting novel phenomena such as the orbital Hall effect [4–14] and the charge-to-orbital conversion via the orbital Rashba-Edelstein effect [15–18]. In analogy with their spin counterparts, these effects enable the electrical manipulation of the orbital degrees of freedom without a mediating interaction like the spin-orbit coupling, opening the possibility of using light elements in novel sustainable devices [19] and reigniting the interest in orbitronics [20,21]. Novel experimental studies have demonstrated that the orbital Hall effect (OHE) can arise in three-dimensional (3D) systems even if the orbital angular momentum of the system vanishes in equilibrium [22,23] and the orbital currents may have very large decay lengths [24,25].

Furthermore, it has been shown that the OHE can induce magnetization dynamics via the orbital torque in magnetic heterobilayers [26–29]. Also, the reciprocal version of this effect, orbital pumping, in which an oscillating magnetic moment creates an orbital current, was recently confirmed [30,31]. In the case of 2D materials, the interplay between their band structure, their orbital degrees of freedom, and the presence of sizable Berry curvature pockets in reciprocal space has garnered significant attention. Theoretical works have shown that, like their 3D counterparts, multiorbital 2D materials can host orbital textures that trigger a sizable OHE [32]. Additionally, several theoretical works predicted that monolayers [12,33,34] and bilayers [35,36] of transition metal dichalcogenides (TMDs) exhibit the OHE within their energy gap and are characterized by an orbital Chern number. Furthermore, these materials exhibit orbital currents that flow through their edge states, which were previously considered trivial from the $\mathbb{Z}_2$ perspective [37,38].

Recently, a theoretical work by Costa *et al.* [39] demonstrated the connection between the orbital Hall insulating phase of certain transition metal dichalcogenide monolayers and their high-order topological insulating phases [40–42], hinting at a connection between the nontopological edge states and the orbital Hall conductivity plateaus [33–36], and evinced the existence of the OHE in centrosymmetric systems. They showed that the accumulation of orbital angular momentum can occur at the edges of ribbons of these materials due to the presence of metallic states that depend on the ribbon orientation.

The development of orbitronic devices based on 2D materials requires a robust criterion to identify orbital-Hall-capable materials. Recent studies by Han *et al.* took a significant step toward this goal [43,44]. The authors conducted a detailed analysis of the microscopic origin of the orbital textures and uncovered the interplay between crystalline and orbital

---

*Contact author: anderson.barbosa@ufrpe.br
†Contact author: tgrappoport@fisica.uminho.pt

085412-1

symmetries that promote hybridizations leading to the emergence of these textures. From another perspective, Eck *et al.* [45] recently presented the conditions that enable the appearance of 2D high-order topological insulators (HOTIs) on the triangular lattice from the interplay between the crystalline and orbital symmetries. Our current study further explores the correlation between orbital hybridization, orbital symmetries, and the OHE to gain insights into its connection to various topological phases.

In this study, we build upon the prior research by Eck *et al.* to investigate how symmetry reduction can induce various spin and orbital topological phases. Specifically, we examine the d_{z^2}, d_{xy}, and $d_{x^2-y^2}$ orbitals within the d subshell on a triangular lattice. This lattice configuration is commonly used to model transition metal dichalcogenide monolayers, offering controllable symmetries by selectively removing certain hopping elements.

We diverged from the norm by fixing the spin-orbit coupling (SOC) and adjusting the hopping terms, illustrating the influence of crystal field competition on band inversion and topological phase transitions, contrary to conventional studies that typically increase SOC while keeping other terms constant. Using this flexibility, we explore diverse topological phases and assess them through quantum transport calculations of both orbital and spin conductivities using Kubo and Landauer-Büttiker formalisms.

By integrating these methodologies, we examine the interaction between orbital and spin Hall conductivities across distinct topological phases and their susceptibility to disorder. For high-order topological insulators, as referenced in prior works, we identify characteristic orbital-Hall conductivity plateaus within the insulating gap.

Additionally, to assess and determine whether the metallic edge states that emerge within the gap upon specific lattice terminations can effectively transport orbital angular momentum, we have devised a mesoscopic device connected to four semi-infinite terminals. Utilizing the Landauer-Büttiker formula, we conduct comprehensive calculations of the orbital and spin Hall conductivities within this mesoscopic device featuring zigzag and flat edges to evaluate how disorder influences the transport of orbital angular momentum in device configurations.

This article is structured as follows: in Sec. II, we introduce the three-band model, discuss its symmetry, and establish its connection to a p orbital model. In Sec. III, we outline four distinct topological phases along with their primary characteristics. We also compute the orbital and spin Hall conductivity of periodic systems using the Kubo formula approach. Finally, in Sec. IV, we explore mesoscopic devices via Landauer-Büttiker calculations to investigate the role of edge states in orbital Hall conductivity and the impact of disorder on the orbital Hall plateau.

II. THE MODEL

We begin with the three-band tight-binding model, which is commonly used to describe the low-energy behavior of H-TMDs. In this model, a triangular lattice accommodates the d_{z^2}, d_{xy}, and $d_{x^2-y^2}$ orbitals. To simplify the analysis, we adopt the same tight-binding parameters as in Ref. [46] for MoS$_2$,

but with a spin-orbit coupling strength that is 15 times larger than the original value. This allows us to transition between different phases of the system by simply removing some of the original hopping elements, which modifies the symmetries of the model without altering the values of the other parameters. Using the basis $\{d_{z^2}, d_{xy}, d_{x^2-y^2}\}$, the Hamiltonian of the system can be written as $\mathcal{H} = \sigma_0 \bigotimes H_0 + H_{\text{SOC}}$, where

$$H_0 = \begin{bmatrix} h_0 & h_1 & h_2 \\ h_1^* & h_{11} & h_{12} \\ h_2^* & h_{12}^* & h_{22} \end{bmatrix}, \qquad (1)$$

with

$$h_0 = 2t_0(\cos 2\alpha + 2\cos\alpha\cos\beta) + \epsilon_1,$$

$$h_1 = -2\sqrt{3}t_2\sin\alpha\sin\beta + 2it_1(\sin 2\alpha + \sin\alpha\cos\beta),$$

$$h_2 = 2t_2(\cos 2\alpha - \cos\alpha\cos\beta) + 2\sqrt{3}it_1\cos\alpha\sin\beta,$$

$$h_{11} = 2t_{11}\cos 2\alpha + (t_{11} + 3t_{22})\cos\alpha\cos\beta + \epsilon_2,$$

$$h_{22} = 2t_{22}\cos 2\alpha + (3t_{11} + t_{22})\cos\alpha\cos\beta + \epsilon_2,$$

$$h_{12} = \sqrt{3}(t_{22} - t_{11})\sin\alpha\sin\beta + 4it_{12}\sin\alpha(\cos\alpha - \cos\beta),$$

$$\alpha = \frac{1}{2}k_x a, \qquad \beta = \frac{\sqrt{3}}{2}k_y a. \qquad (2)$$

This is a symmetry-based tight-binding Hamiltonian that does not originate from a Slater-Koster approach, as the hopping elements between the d orbitals are mediated by the p orbitals of the chalcogens in 2H-TMDs. By examining the TMD Hamiltonian, it becomes apparent that, apart from the term proportional to t_2, Eq. (1) is formally equivalent to a Slater-Koster Hamiltonian utilizing p_x, p_y, and p_z orbitals with basis $\{p_z, p_x, p_y\}$ in a two-dimensional triangular lattice in which the inversion and mirror symmetries of the lattice are broken (see Appendix A).

In this map between the two Hamiltonians, t_0, t_{11}, and t_{22} are Slater-Koster hopping elements for the σ and π bonds for p_z, p_x, and p_y orbitals that respect all the symmetries of a two-dimensional triangular lattice. The terms proportional to t_0, t_{11}, and t_{22} describe the nearest-neighbor hopping in a triangular lattice of layer group $p6/mmm$, which is generated by a sixfold rotation, three vertical reflection planes σ_v, three diagonal reflection planes σ_d, and one horizontal reflection plane σ_h [45].

If inversion symmetry is broken, the sixfold rotation (C_6) reduces to C_3, and the Hamiltonian presents the term proportional to t_{12}. On the other hand, if only the mirror symmetry with respect to the plane is broken, it is possible to have hybridization between p_z and the in-plane orbitals p_x and p_y, which gives rise to the term proportional to t_1. The extra term proportional to t_2 is the only one that cannot be mapped into a Slater-Koster Hamiltonian. It is important to note, however, that although we can formally map one Hamiltonian into another, the meaning of the different terms is not the same for the d orbitals. For instance, t_1 hybridizes orbitals belonging to different irreducible representations, as in the case of the p orbitals, but does not break the same mirror symmetry, which is preserved in 2H-TMD monolayers.
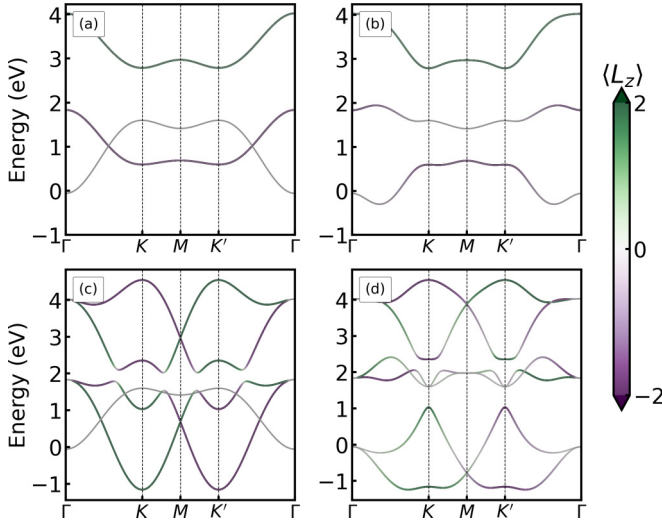
FIG. 1. Bulk energy bands of the four topological phases of the three-band model for various terms in the Hamiltonian. (a) Phase I: $t_1 = t_2 = t_{12} = 0$. (b) Phase II: $t_2 = t_{12} = 0, t_1 \neq 0$. (c) Phase III: $t_1 = t_2 = 0, t_{12} \neq 0$. (d) Phase IV: $t_1 \neq t_2 \neq t_{12} \neq 0$. The colors indicate the L_z character of each band; for phases I and II, where the inversion symmetry is preserved, only the energy states corresponding to the $S_z = \uparrow$ sector are shown.

The spin-orbit coupling is written as

$$H_{\text{SOC}} = \sigma_z \frac{\lambda}{2} \begin{bmatrix} 0 & 0 & 0 \\ 0 & 0 & 2i \\ 0 & -2i & 0 \end{bmatrix}. \tag{3}$$

Here, λ is the strength of the spin-orbit coupling, and σ_0 and σ_z are the 2×2 identity matrix and the z Pauli matrices, respectively. To investigate the connection between topology and the orbital Hall plateau, we analyze four different phases. To consider the different phases without modifying the spin-orbit coupling or the strength of the other hoppings, we take a λ that is 15 times stronger than the SOC of MoS$_2$. The band structures of the four phases together with their orbital characters are shown in Fig. 1. The orbital character of the energy states is computed as $\langle L_z^{n,s}(\mathbf{k}) \rangle = \langle \psi_{n,s}(\mathbf{k}) | \hat{L}_z | \psi_{n,s}(\mathbf{k}) \rangle$, where $|\psi_{n,s}(\mathbf{k})\rangle$ is the nth energy band with spin $s = \uparrow, \downarrow$ evaluated at $\mathbf{k}$. For phase I, $t_1 = t_2 = t_{12} = 0$, which, in the case of p orbitals, is equivalent to a system in which all the symmetries of the triangular lattices are kept. Figure 1(a) shows the band structure of the phase with the orbital character of the energy states within the $S_z = \uparrow$ sector. For this case, the subspace for $m_l = 0$ is separated from the subspace where $m_l = \pm l$. Because of the inversion symmetry, all bands are spin degenerate. The system has a lower band with $m_l = 0$. The two other bands that belong to the $m_l \pm l$ subspace are split by the spin-orbit coupling. For phase II, in the case of p orbitals, the mirror symmetry is broken with $t_1 = t_2 = 0$ and $t_{12} \neq 0$ while preserving the inversion symmetry and, consequently, the spin-degenerate energy bands. However, there is a finite hybridization between the bands belonging to the $m_l = \pm l$ subspace and the one for $m_l = 0$. As a result, the band structure of Fig. 1(b) presents a gap at the band crossing of Fig. 1(a).
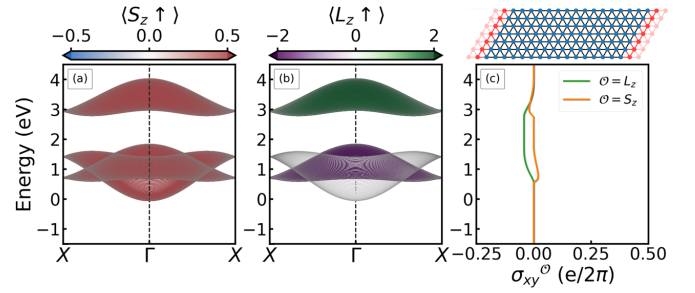
In the case of phase III, the subspaces of $m_l = \pm l$ and $m_l = 0$ are decoupled, but the inversion symmetry is broken. As a result, the bands in Fig. 1(c) can present spin and orbital angular momentum textures. This breaks the spin degeneracy of the bands belonging to the $m_l = \pm l$ subspace. Phase IV presents all the parameters of a three-band model for MoS$_2$ so that all hoppings of the Hamiltonian are finite and a much stronger spin-orbit coupling produces a large splitting of the conduction band states, as seen in Fig. 1(d), but still keeps the spin and orbital character of the TMDs in the vicinity of the band gap.

III. TOPOLOGY AND THE SPIN AND ORBITAL ANGULAR MOMENTUM TRANSPORT

To explore the topology of the different phases, we use a twofold approach: we calculate the band structure of a nanoribbon (shown in the insets of Figs. 2–5) and analyze the edge states for the four different phases while comparing them with the spin and orbital Hall conductivities of the bulk system. For the computation of the spin and orbital Hall conductivities, we used the Kubo-Bastin
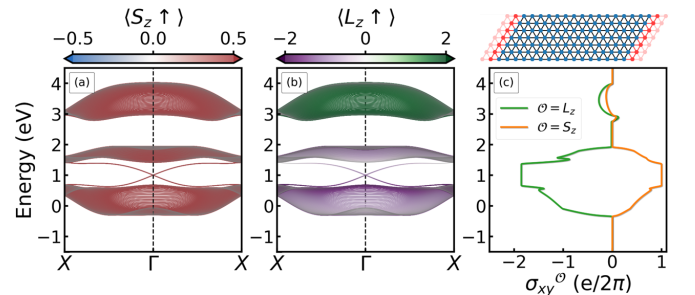

FIG. 2. (a) Spin and (b) orbital character of the spin-up energy bands of a nanoribbon with breadth $W = 50\vec{a}_2$ for a system in phase I. (c) Top: Schematic representation of the ribbons used in the calculation of the energy states shown in (a) and (b); the red color signals the periodic direction of the ribbon. Bottom: Spin (orange) and orbital (green) Hall conductivities for a system in phase I.

FIG. 3. (a) Spin and (b) orbital character of the spin-up energy bands of a nanoribbon with breadth $W = 50\vec{a}_2$ for a system in phase II. (c) Top: Schematic representation of the ribbons used in the calculation of the energy states shown in (a) and (b); the red color signals the periodic direction of the ribbon. Bottom: Spin (orange) and orbital (green) Hall conductivities for a system in phase II.
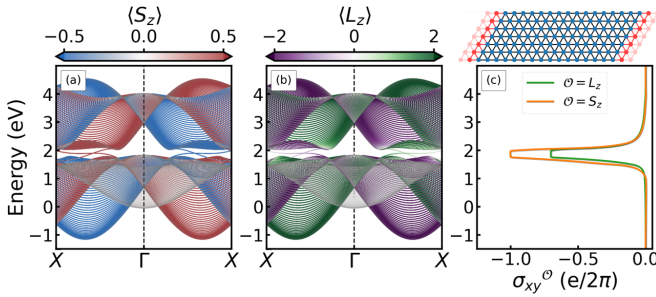
FIG. 4. (a) Spin and (b) orbital character of the energy bands of a nanoribbon with breadth $W = 50\bar{a}_2$ for a system in phase III. (c) Top: Schematic representation of the ribbons used in the calculation of the energy states shown in (a) and (b); the red color signals the periodic direction of the ribbon. Bottom: Spin (orange) and orbital (green) Hall conductivities for a system in phase III.

formula [47–49]:

$$
\begin{aligned}
\sigma_{\alpha\beta}^{\mathcal{O}}(\mu, T) = & ie\hbar \int_{-\infty}^{\infty} d\varepsilon f(\varepsilon, \mu, T) \\
& \times \text{Im}\big[\text{Tr}\langle J_{\alpha}^{\mathcal{O}}\delta(\varepsilon - H)v_{\beta}\partial_{\varepsilon}G^{+}(\varepsilon)\rangle\big], \quad (4)
\end{aligned}
$$

where $J_{\alpha}^{\mathcal{O}} = \frac{1}{2\Omega}\{v_{\alpha}, \mathcal{O}\}$ is the angular momentum current density operator, with $\mathcal{O}$ being either the S_z spin operator or the L_z orbital angular momentum operators, where the latter is evaluated within the atom-centered approximation; v_{α} being the α component of the velocity operator in $v_{\alpha} = -\frac{i}{\hbar}[H, R_{\alpha}]$, where R_{α} is the projection of along the α direction of the position operator and H is the Hamiltonian of the system; and Ω being the area of the sample. $G^{+}(\varepsilon)$ and $\delta(\varepsilon - H)$ are the retarded Green's and spectral functions, respectively. These are approximated using the kernel-polynomial method [50,51] as implemented in the LSQUANT tool kit [52]. For all of our transport calculations, we used 1024 Chebyshev moments with the Jackson kernel to obtain an energy resolution of $\delta \approx 3$ meV, while assuming periodicity allowed us to consider a grid of 512×512 points in reciprocal space.

Starting with phase I, Figs. 2(a) and 2(b) show the band structure of a nanoribbon, with the color codes indicating the
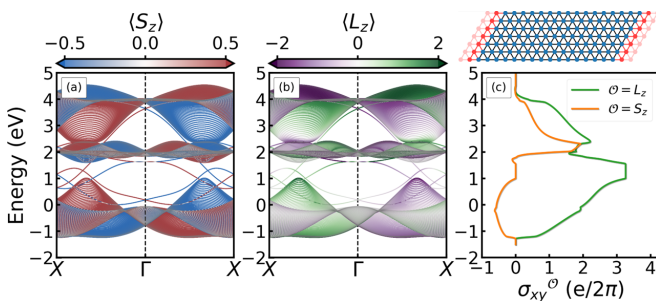

FIG. 5. (a) Spin and (b) orbital character of the energy bands of a nanoribbon with breadth $W = 50\bar{a}_2$ for a system in phase IV. (c) Top: Schematic representation of the ribbons used in the calculation of the energy states shown in (a) and (b); the red color signals the periodic direction of the ribbon. Bottom: Spin (orange) and orbital (green) conductivity for a system in phase IV.

S_z and L_z projections, respectively. Because of the spin degeneracy, we are showing the spin and orbital characters of the energy states within the $S_z = \uparrow$ sector. The band structure of the nanoribbon does not have in-gap edge states, signaling that the system lies in a topologically trivial state. Additionally, from the spin and orbital projection of the energy states of the nanoribbon, it is clear that the vanishing contribution from hoppings t_1, t_2, and t_{12} forbids the hybridization between the orbitals with d_{z^2}, $d_{x^2-y^2}$, and d_{xy} and makes the system inversion symmetric. Consequently, the SOC enforces the energy states formed by linear combinations of orbitals $d_{x^2-y^2}$ and d_{xy} to have a well-defined atomic angular momentum character [see also Fig. 11(a)], thus making the system a trivial SOC insulator, as negligible orbital and spin Hall conductivities presented in Fig. 2(c) confirm.

For phase II, the band structure of the nanoribbon in Figs. 3(a) and 3(b) shows that after enabling the hybridization between the orbitals d_{z^2}, d_{xy}, and $d_{x^2-y^2}$ through t_1 while maintaining $t_2 = t_{12} = 0$, the system exhibits inversion symmetry with two pairs of in-gap spin-polarized edge states. Interestingly, the orbital angular momentum character of the spin-up states [Fig. 3(b)] unveils that the combined action of the SOC and orbital hybridization results in the mixing of d_{z^2} states and $m_{-l} = \frac{1}{\sqrt{2}}(d_{x^2-y^2} - id_{xy})$ states, which resembles the Bernevig-Hughes-Zhang (BHZ) model of quantum spin Hall insulators, and consequently, the edge states of this system carry opposite spin and orbital angular momenta. The quantized spin Hall conductivity characterizes the topological insulator, and the opposite bulk spin and orbital Hall conductivities shown in Fig. 3(c) confirm the relation with the BHZ model.

To further inquire into the effects of the orbital hybridization on the appearance of topologically nontrivial phases, for phase III, we follow a similar analysis as we did for phase II. Figures 4(a) and 4(b) show the band structure and the respective spin and orbital characters of the states of the nanoribbon. Here, we forbid the hybridization of the orbitals d_{z^2} with $d_{x^2-y^2}$, d_{xy} by setting the hoppings $t_1 = t_2 = 0$, and we break the inversion symmetry by allowing $t_{12} \neq 0$. Analyzing the orbital and spin character of the edge states of the system, we can see that the $d_{x^2-y^2}$ and d_{xy} orbitals are responsible for the nontrivial topological properties of the system, whereas the states related to d_{z^2} are effectively decoupled. In contrast with phase II, the hybridization and the inversion symmetry breaking favor the appearance of pairs of edge states with different spin and orbital characters at opposite sides of the ribbon Brillouin zone, in relation to spin- and orbital-valley locking. Similarly, as before, these edge states are endowed with sizable orbital angular momentum, providing these states with additional topological protection since any backscattering event would require a change in not only the spin character but also the orbital part. The spin and orbital Hall conductivities shown in Fig. 3(c) confirm the topologically nontrivial nature of this phase, and the spin and orbital Hall plateaus have the same sign, in contrast to phase II.

Finally, for phase IV, we allow all the hopping terms, and essentially, the model reduces to the three-band model for 2Hf-TMDs presented by Liu *et al.* [46], but with enhanced spin-orbit coupling. By analyzing the spin and orbital characters of the energy states of the nanoribbon shown in Figs. 5(a)

and 5(b), respectively, we find that the system presents edge states within its main energy gap. They are similar to the edge states presented in MoS_2 [33,35] but have large splitting from the strong spin-orbit coupling. There are four pairs of edge states, so the system is topologically trivial from the $\mathbb{Z}_2$ classification and exhibits a behavior that is drastically different from the previous phases. One can notice that the spin character of the edge states on a single side of the ribbon Brillouin zone contains opposite spin polarizations, in contrast to the energy states shown in Fig. 4(a). However, when focusing on the orbital character of the edge states of this system, we found that they retain a similar orbital character, as shown in Fig. 4(b). These properties correlate with the absence of spin Hall conductivity plateaus within the energy gap but the presence of the orbital Hall insulating phase, as shown in Fig. 5(c), which is characterized by an orbital Chern number of 1 [35]. The even number of edge state pairs in the case of flat termination together with the absence of edge states for zigzag edges is consistent with a higher-order topological phase, which is present in this case [53].

Although we do not explore the topological phase transition between these phases, they occur with the usual band closing and reopening. The order parameter of phases II and III is the ($\mathbb{Z}_2$) topological invariant [54]. Here, as the spin is a good quantum number, it translates into a quantized spin Hall conductivity, and the bulk-edge correspondence can be seen in the number of edge states crossing the insulating gap in phases II and III. The HOTI in phase IV can be characterized by the topological indicator $\chi^{(3)}$ and corner charge Q_c^3 [40]. For noncentrosymmetric materials, the HOTI phase is protected by C_n rotation symmetry [40,55–57]. This phase can be identified using the symmetry representations of the occupied energy bands at specific high-symmetry points in the first Brillouin zone. For C_3 rotation symmetry, we define $[K_p^{(3)}]$ as $\#K_p^{(3)} - \#\Gamma_p^{(3)}$, where $\#K_p^{(3)}$ and $\#\Gamma_p^{(3)}$ denote the number of occupied bands with symmetry eigenvalue $e^{2\pi i(p-1)/3}$ (for $p = 1, 2, 3$) at the K and Γ points, respectively. The topological indicator $\chi^{(3)}$ and the corresponding corner charge $Q_c^{(3)}$ are given by

$$\chi^{(3)} = \left([K_1^{(3)}], [K_2^{(3)}]\right), \quad Q_c^{(3)} = \frac{e}{3}[K_2^{(3)}] \mod e,$$

where e is the elementary charge. Since the orbital angular momentum L_z is the generator of the rotations, one can see that the rotation eigenvalues $e^{2\pi i(p-1)/3}$ (for $p = 1, 2, 3$) correspond to the eigenvalues of the operator L_z with $m_z = 0, 1, -1$, respectively. Therefore, analyzing the orbital character of the valence bands depicted in Fig. 1(d), we find that the topological indicators and fractional charges are given by $\chi^{(3)} = (-1, 2)$ and $Q_c^{(3)} = 2e/3$, in agreement with the results from Ref. [39].

IV. THE ORBITAL HALL CONDUCTIVITY OF NANORIBBONS: LANDAUER-BüTTIKER CALCULATIONS

We proceed to further analyze the higher-order topological phase and check whether the edge states possess the capability of carrying orbital angular momentum. To accomplish this, we designed an OHE setup consisting of a mesoscopic device connected to four semi-infinite terminals subjected to
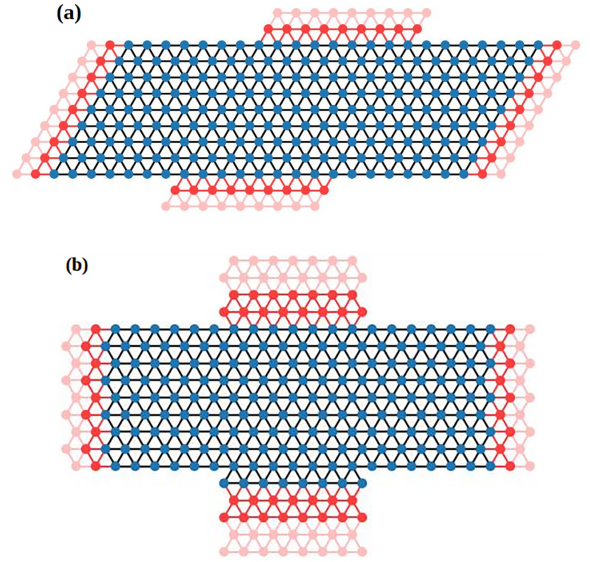

FIG. 6. (a) Triangular lattice device with flat edges. (b) Triangular lattice device with flat and zigzag edges. The scattering region (blue) is connected to four leads semi-infinite leads (red).

voltage biases V_i. In our calculations, we considered two distinct device geometries. Figure 6(a) showcases a configuration with all flat edges, whereas Fig. 6(b) presents a conventional Hall-bar geometry characterized by a combination of flat and zigzag edges.

In the Landauer-Büttiker formalism, the orbital (spin) projected current through the ith terminal in the linear regime at low temperature is given by

$$I_{i,\eta}^{\mathcal{O}} = \frac{e^2}{h} \sum_j \tau_{ij,\eta}^{\mathcal{O}}(V_i - V_j), \tag{5}$$

with $\mathcal{O}$ being one of the L_z orbital angular momenta or S_z spin states [$\circlearrowleft (\uparrow)$ or $\circlearrowright (\downarrow)$]. The orbital (spin) transmission coefficient is calculated from the scattering matrix $\mathcal{S} = [\mathcal{S}_{ij}]_{i,j=1,...,4}$ as

$$\tau_{ij,\eta}^{\mathcal{O}} = \mathbf{Tr}\left[(\mathcal{S}_{ij})^\dagger \mathcal{P}_\eta^{\mathcal{O}} \mathcal{S}_{ij}\right], \tag{6}$$

where the matrices $\mathcal{P}_\eta^{L_\eta} = \mathbb{1}_N \otimes l^\eta \otimes \sigma^0$ and $\mathcal{P}_\eta^{S_\eta} = \mathbb{1}_N \otimes l^0 \otimes \sigma^\eta$ are projectors and $\mathbb{1}_N$ is an identity matrix with dimensions $N \times N$. The dimensionless integer N refers to the number of propagating wave modes in the terminals, proportional to the terminal width W and the Fermi vector k_F, computed through the equation $N = k_F W/\pi$. The matrices l^η and σ^η, with $\eta = \{x, y, z\}$, are the orbital angular momentum and spin matrices, respectively, and the cases with $\eta = 0$ refer to the identity matrices in the orbital and spin subspaces. Thus, by setting either $\eta = 0$ or $\eta = \{x, y, z\}$, the charge and orbital (spin) can be respectively addressed.

The pure orbital Hall conductivity (OHC) and spin Hall conductivity (SHC) $I_{i,z}^{L_z(S_z)} = \frac{\hbar}{e}(I_i^{\circlearrowleft(\uparrow)} - I_i^{\circlearrowright(\downarrow)})$, $i = 3, 4$, can be obtained by assuming that the charge current vanishes in the transverse terminals, $I_{i,0}^c = I_i^{\circlearrowleft(\uparrow)} + I_i^{\circlearrowright(\downarrow)} = 0$, but is conserved in the longitudinal terminals, $I_{1,0}^c = -I_{2,0}^c = I^c$ [58–60]. By applying these conditions to Eq. (5), we
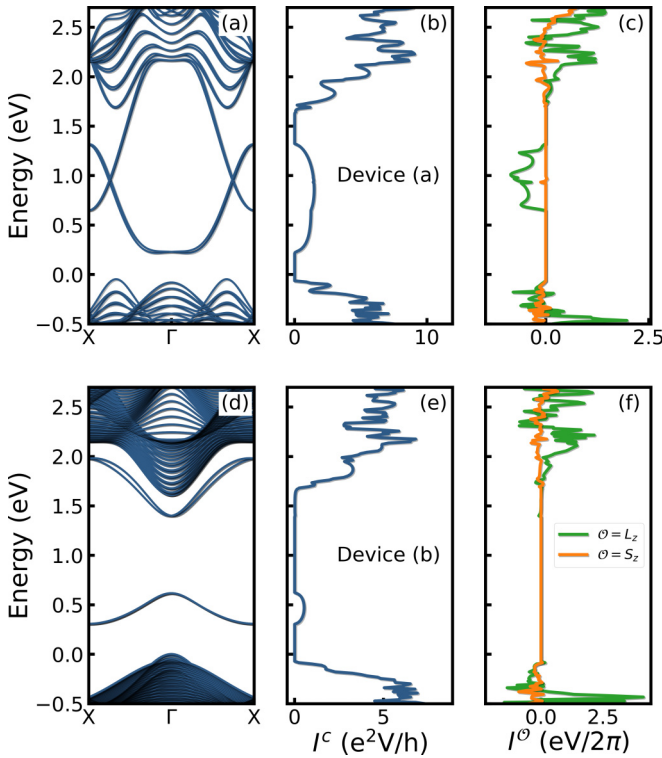
FIG. 7. (a) Band structure, (b) charge current, and (c) orbital and spin Hall current of a mesoscopic device with the dimensions and design of Fig. 6(a). (d) Band structure, (e) charge current, and (f) orbital and spin Hall current of a mesoscopic device with the dimensions and design of Fig. 6(b). (c) and (f) Spin (orange) and orbital (green) conductance for a MoS_2 monolayer, which is in phase IV.
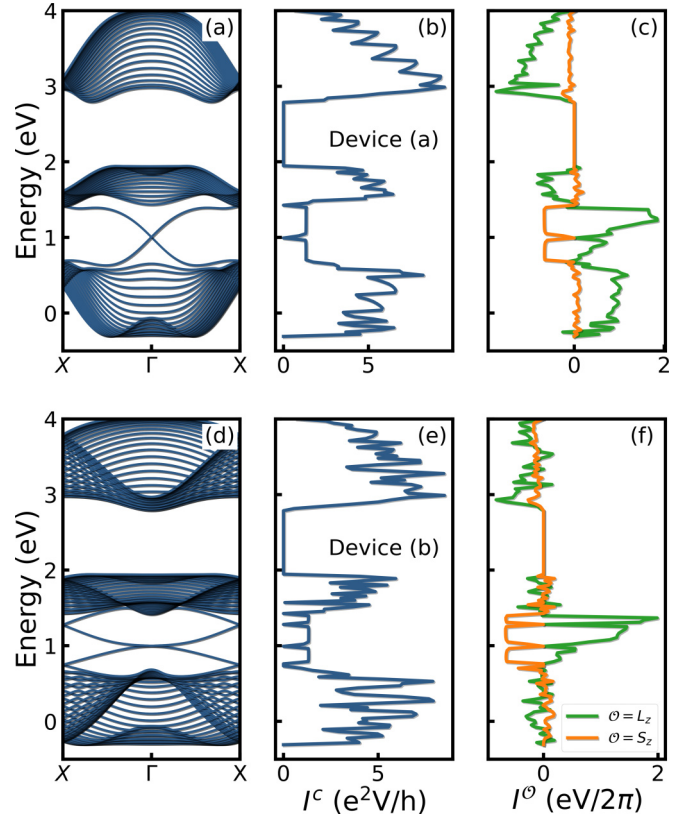

FIG. 8. (a) Band structure, (b) charge current, and (c) orbital and spin Hall current of a mesoscopic device with the dimensions and design of Fig. 6(a). (d) Band structure, (e) charge current, and (f) orbital and spin Hall current of a mesoscopic device with the dimensions and design of Fig. 6(b). (c) and (f) Spin (orange) and orbital (green) current, which is in phase II.

obtain [10]

$$I_{i,\eta}^{\mathcal{O}} = \frac{e}{2\pi}\left[\left(\tau_{i2,\eta}^{\mathcal{O}} - \tau_{i1,\eta}^{\mathcal{O}}\right)\frac{V}{2} - \tau_{i3,\eta}^{\mathcal{O}}V_3 + \tau_{i4,\eta}^{\mathcal{O}}V_4\right] \qquad (7)$$

for $i = 3, 4$, where V is a constant potential difference between longitudinal terminals and $V_{3,4}$ is the transversal terminal voltage.

We begin our investigation by examining the influence of ribbon termination on the orbital Hall conductance in a higher-order topological insulator. To facilitate a clearer visualization of the role of in-gap edge states in orbital transport, we utilize a triangular lattice with parameters akin to MoS_2, which belongs to the same topological phase as phase IV. The numerical calculations in this section were implemented in the KWANT software [61].

It is essential to note that to establish a connection between the edge states of the original honeycomb lattice of MoS_2 and the triangular lattice of d orbitals, the zigzag edge of the honeycomb lattice corresponds to the flat edge of the triangular lattice, which consists of one of the sublattices. Simultaneously, the armchair edge of the honeycomb lattice is associated with the zigzag edge of the triangular lattice.

Figure 7(a) presents the band structure of the type of device sketched in Fig. 6(a) for the parameters of MoS_2. In that device, all edges break the threefold rotation symmetry of the triangular lattice. The band structure of the system is very similar to the band structure of a MoS_2 nanoribbon in the three-orbital approximation [39]. Figure 7(b) presents the longitudinal charge current of the device, where it is clear that the in-gap edges are metallic and can conduct charge. Figure 7(c) depicts the transverse spin and orbital currents. While the spin current is zero inside the gap, we can see a finite orbital current in the same energy window of the in-gap edge states. In contrast, if the device also presents some edges that preserve the threefold rotation symmetry of the triangular lattice, as sketched in Fig. 6(b), the band structure remains similar, as shown in Fig. 7(d), but the charge current is suppressed in a good part of the energy window inside the gap [Fig. 7(e)], and the system does not present either spin or orbital currents, as shown in Fig. 7(f).

This behavior can be compared with the characteristics of a first-order topological insulator, such as the one in phase II. Figure 8(a) presents the band structure for the device sketched in Fig. 6(a) for a topological insulator in phase II discussed previously. Figure 8(b) presents the longitudinal charge current of the device, and it is clear that the in-gap edges are metallic and can conduct charge. Figure 8(c) depicts the transverse spin and orbital currents. Both spin and orbital currents are finite with opposite signs. While the spin current has a clear plateau inside the gap, the orbital current does not seem to have a quantized value. Figures 8(d)–8(f) present the same
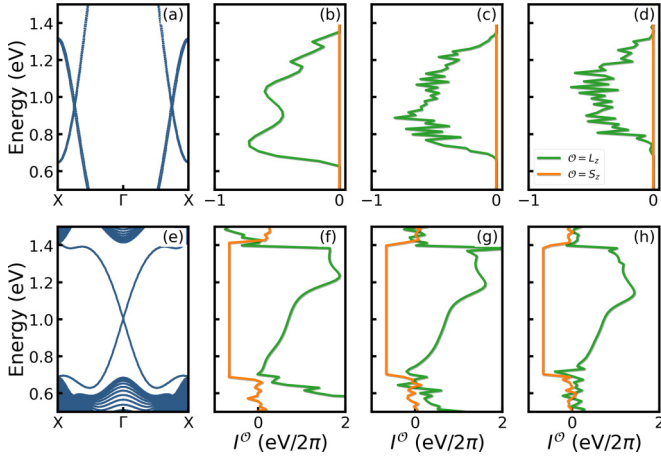
FIG. 9. (a) Band structure and orbital and spin Hall current with disorder strengths for (b) $U = 0$, (c) $U = 0.1$ eV, (d) $U = 0.2$ eV for a mesoscopic device of a MoS_2 monolayer which is in phase IV with dimensions 10 times bigger than as shown in Fig. 6(a). (e) Band structure and orbital and spin Hall current with disorder strengths for (f) $U = 0$, (g) $U = 0.1$ eV, (h) $U = 0.2$ eV of a mesoscopic device which is in phase II with dimensions 10 times bigger than as shown in Fig. 6(a).

results, but for the device sketched in Fig. 6(b). Different from the previous cases, the results are robust independent of the type of edges the device presents, underlying the importance of topological protection by a global symmetry.

Finally, to study the robustness of the orbital and spin Hall currents against scalar disorder, we included an Anderson disorder term that varies randomly from site to site according to a uniform distribution in the interval $(-U/2, U/2)$, with U being the disorder strength. Figures 9(b)–9(d) present both the orbital and spin Hall currents of MoS_2 for $U = 0$, $U = 0.1$ eV, and $U = 0.2$ eV, respectively. From these plots, one can notice that the orbital Hall currents are not protected against disorder. Although the plateau observed in bulk calculations survives with increasing disorder [13], our results show a decrease in the orbital Hall current. For the case of the topological insulator of phase II, Figs. 9(f)–9(h) show that the spin currents are not affected by the increment of the disorder, as one would expect for topologically protected states. In contrast, the orbital Hall currents are affected by the disorder.

V. CONCLUSION

To summarize, our study focused on a generalized multiorbital tight-binding model on a triangular lattice. This system was recently used to obtain higher-order topological phases in two-dimensional materials but also is especially relevant for modeling transition metal dichalcogenide monolayers. By modifying the hopping terms of the model, we changed the hybridization between orbitals and uncovered the intricate interplay between spin-orbit coupling and various symmetry-breaking mechanisms, which led to the identification of four distinct topological phases [45]. Notably, this interplay also resulted in the emergence of an orbital Hall effect with unique characteristics. For the two first-order topological phases, the quantized spin Hall conductivity is accompanied by a nonquantized orbital Hall plateau, while the higher-order

topological phase presents the orbital Hall effect in the absence of the spin Hall effect.

Furthermore, we applied the Landauer-Büttiker formula to establish that in the orbital Hall insulating phase, the orbital angular momentum is carried by edge states that exist in nanoribbons with flat terminations. Importantly, we demonstrated that these edge states lack the topological protection against disorder observed in the edge states associated with a first-order topological insulator. These findings provide valuable insights into the behavior of edge states in systems with higher-order topology and their role in the onset of the orbital Hall effect in these systems.

APPENDIX A: SLATER-KOSTER APPROACH FOR *p* ORBITALS IN A TRIANGULAR LATTICE

To calculate the first-neighbor hoppings of a Hamiltonian of p orbitals in a triangular lattice, we define $n_z = \cos\theta$, $n_x = \cos\phi\sin\theta$, and $n_y = \sin\phi\sin\theta$.

For the hopping between p orbitals one has

$$t_{p_i, p_i} = n_i^2 V_{pp\sigma} + (1 - n_i^2) V_{pp\pi}, \tag{A1}$$

$$t_{p_i, p_j} = n_i n_j (V_{pp\sigma} - V_{pp\pi}), \tag{A2}$$

with $i = x, y, z$ and $i \neq j$.

For the two-dimensional lattice, we define $n_z = \cos\theta = 0 = 1$, $n_x = \cos\phi$, and $n_y = \sin\phi$ and $t_{p_z, p_z} = n_i^2 V_{pp\sigma}^z$. Using $\cos(\pi/3) = \cos(-\pi/3) = -\cos(2\pi/3) = -\cos(-2\pi/3) = \frac{1}{2}$, $\sin(\pi/3) = -\cos(-\pi/3) = \sin(2\pi/3) = -\sin(-2\pi/3) = \frac{\sqrt{3}}{2}$, $\cos(0) = -\cos(\pi) = 1$, and $\sin 0 = \sin(\pi) = 0$, one can construct the hopping elements that preserve all the symmetries of the lattice:

$$\begin{aligned} h_{p_x, p_x}(k_x, k_y) = &\frac{1}{4}(V_{pp\sigma} + 3V_{pp\pi})(e^{i(\alpha+\beta)} + e^{-i(\alpha+\beta)a} \\ &+ e^{i(\alpha-\beta)} + e^{-i(\alpha-\beta)}) \\ &+ V_{pp\sigma}(e^{2i\alpha} + e^{-2i\alpha}), \end{aligned} \tag{A3}$$
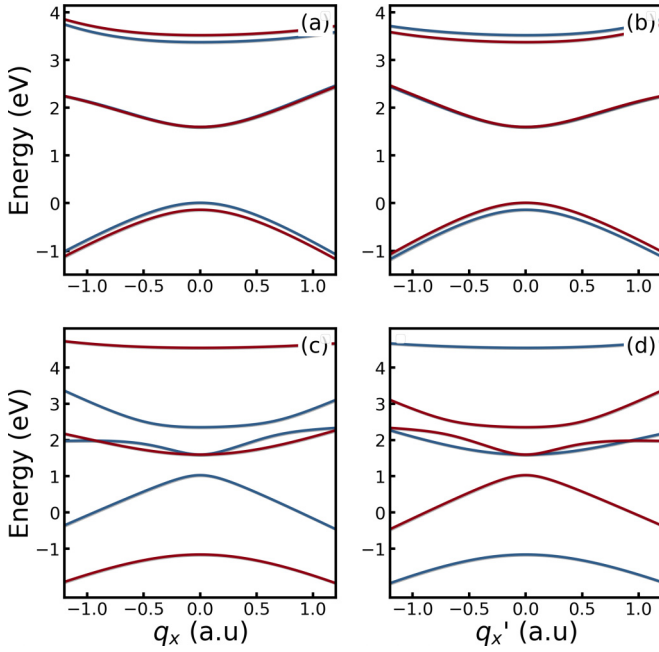
FIG. 10. Band structure of the three-band low-energy model for the parameters of the three-band model of MoS$_2$ in the vicinity of Dirac points (a) K and (b) K'. (c) and (d) The band structures for the parameters of phase IV.

$$h_{p_x,p_x}(k_x, k_y) = (V_{pp\sigma} + 3V_{pp\pi})\cos\alpha\cos\beta + 2V_{pp\sigma}\cos 2\alpha,$$
$$(A4)$$

$$h_{p_y,p_y}(k_x, k_y) = (3V_{pp\sigma} + V_{pp\pi})\cos\alpha\cos\beta + 2V_{pp\pi}\cos 2\alpha.$$
$$(A5)$$

Using the expressions above, one has $\cos(\pi/3)\sin(\pi/3) = -\cos(-\pi/3)\sin(-\pi/3) = \cos(-2\pi/3)\sin(-2\pi/3) = -\cos(2\pi/3)\sin(2\pi/3) = \frac{\sqrt{3}}{4}$ and $\cos(0)\sin(0) = \cos(\pi)\sin(\pi) = 0$, and

$$h_{p_x,p_y}(k_x, k_y) = \frac{\sqrt{3}}{4}(V_{pp\sigma} - V_{pp\pi})(e^{i(\alpha+\beta)} + e^{-i(\alpha+\beta)} - e^{i(\alpha-\beta)} - e^{-i(\alpha-\beta)}),$$
$$(A6)$$

$$h_{p_x,p_y}(k_x, k_y) = -\sqrt{3}(V_{pp\sigma} - V_{pp\pi})\sin\alpha\sin\beta. \quad (A7)$$

As can be seen, if all the symmetries are preserved, the subspace of the p_z orbital is separated from the subspace of the p_x and p_y orbitals. However, if the vertical reflection symmetry is broken, it allows for hybridization between them, which can be given by $t_{p_i p_z} = \lambda_h n_i = -t_{p_z p_i}$,

$$h_{p_x,p_z}(k_x, k_y) = \frac{1}{2}\lambda_h(e^{i(\alpha+\beta)} - e^{-i(\alpha+\beta)} + e^{i(\alpha-\beta)} - e^{-i(\alpha-\beta)} + 2e^{2i\alpha} - 2e^{-2i\alpha}), \quad (A8)$$

$$h_{p_x,p_z}(k_x, k_y) = -2i\lambda_h(\sin 2\alpha + \sin\alpha\cos\beta), \quad (A9)$$

$$h_{p_y,p_z}(k_x, k_y) = \frac{\sqrt{3}}{2}\lambda_h(e^{i(\alpha+\beta)} - e^{-i(\alpha+\beta)} - e^{i(\alpha-\beta)} + e^{-i(\alpha-\beta)}), \quad (A10)$$

$$h_{p_y,p_z}(k_x, k_y) = 2\sqrt{3}i\lambda_h\cos\alpha\sin\beta. \quad (A11)$$

We can also break inversion symmetry by breaking σ_v while still respecting the threefold rotation symmetry. For this purpose, we can introduce a hopping given by $t^v_{p_y,p_x} = \lambda_v\cos(3\phi) = -t^v_{p_x,p_y}$, so that

$$h^v_{p_x,p_y}(k_x, k_y) = \lambda_v\big(-e^{i(\alpha+\beta)} + e^{-i(\alpha+\beta)} - e^{i(\alpha-\beta)} + e^{-i(\alpha-\beta)} + e^{2i\alpha} - e^{-2i\alpha}\big), \quad (A12)$$

$$h^v_{p_x,p_y}(k_x, k_y) = \lambda_v(2i\sin 2\alpha - 4i\sin\alpha\cos\beta), \quad (A13)$$

$$h^v_{p_x,p_y}(k_x, k_y) = 4i\lambda_v\sin\alpha(\cos\alpha - \cos\beta). \quad (A14)$$

APPENDIX B: LOW-ENERGY HAMILTONIAN

To better understand how phase IV is related to the appearance of an orbital Hall plateau in the absence of spin Hall conductivity, it is helpful to look at a simplified low-energy Hamiltonian. Since the original Hamiltonian, H_0, is written in a basis that spans states with orbital angular momentum quantum numbers m_l of $-l$, 0, and l, we can map it to a basis of p orbitals and rewrite it in terms of the orbital angular momentum operators L_x, L_y, and L_z. We can then expand this Hamiltonian around the Dirac points, which is relevant for phase IV.

The Hamiltonian for each valley $H_{K(K')}(q_x, q_y)$, with $\vec{q} = \vec{k} - \vec{K}(\vec{K'})$, reads

$$H_K(q_x, q_y) = \left(-\frac{3}{2}(t_{11} + t_{22}) + \epsilon_2\right)L_z^2 - 3\sqrt{3}t_{12}\tau_z L_z + \lambda s_z L_z$$
$$+ (-3t_0 + \epsilon_1)\left(\frac{L^2}{l(l+1)} - L_z^2\right)$$
$$+ \frac{3\sqrt{3}}{2}t_2\tau_z(q_x L_x - q_y L_y)$$
$$+ \frac{3}{2}t_1\{L_z, (q_x L_x - q_y L_y)\} - \frac{3\sqrt{3}}{4}(t_{11} - t_{22})$$
$$\times [L_x(q_x L_x + q_y L_y) + L_y(q_x L_y - q_y L_x)], \quad (B1)$$

where $\tau_z = \pm 1$ represents the different valleys and s_z is the spin operator. From the equation above, it is clear that up to first order in q_x and q_y the spin-orbit coupling does not produce any spin texture. On the other hand, the last term of the Hamiltonian, proportional to the difference $t_{11} - t_{22}$, is connected to an orbital Rashba coupling while the terms proportional to t_1 and t_2 incorporate an orbital Dresselhaus coupling. Furthermore, t_{12} is responsible for a strong orbital-valley locking when it dominates over other contributions. It becomes clear that the spin-valley coupling that is seen in TMDs is mediated by an orbital-valley coupling.

To test the new low-energy Hamiltonian, we first present the band structure for the parameters of the three-band model of MoS$_2$ in Fig. 10 in the vicinity of the K [Fig. 10(a)] and K' [Fig. 10(b)] Dirac points. The band structure is consistent with both the tight-binding and two-band low-energy models, keeping the spin character of the bands in the two Dirac points while explicitly taking into account the orbital characters of the three states in K and K'. Figures 10(c) and 10(d) show the band structures for the parameters used in phase IV and also provide a consistent description of the bands.

APPENDIX C: SPIN PROJECTION OF THE ENERGY STATES FOR THE FOUR PHASES

To complement the analyses from Fig. 1, we also computed the spin character of the energy bands for the four phases. As before, only one spin sector is shown for phases I and II, which are inversion symmetric. Comparing Fig. 11(a) with Fig. 1(a), it is clear that phase I does not possess any band inversion, which confirms its topologically trivial character. Figure 11(b) evinces that the nontrivial topology arises from the band inversion between the states with $m_z = \pm 2$ and $m_z = 0$, as shown in Fig. 1, evincing the role of the orbital degrees of freedom in the design of topological phases. Moreover, the data from Figs. 11(c) and 1(c) add to this interpretation since the quantum spin Hall insulating state arises in phase III from the band inversion between states with $m_z = \pm 1$. On the other hand, the states with $m_z = 0$ do not hybridize and are insensitive to the SOC. Furthermore, for phase IV, the hybridization between states with $m_z = \pm 1$ and $m_z = 0$ promotes the occurrence of an additional band inversion, driving the system to a topologically trivial state from the $\mathcal{Z}_2$ classification. Nevertheless, it still exhibits an orbital Hall insulating phase.
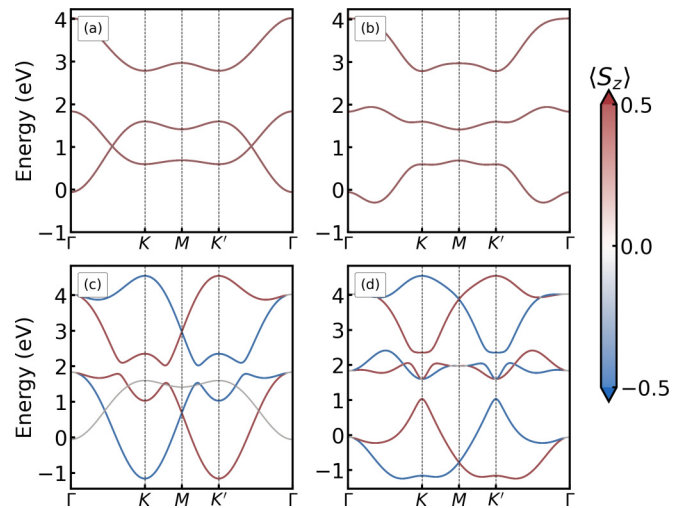

FIG. 11. Bulk energy bands of the four topological phases of the three-band model for various terms in the Hamiltonian. (a) Phase I: $t_1 = t_2 = t_{12} = 0$. (b) Phase II: $t_2 = t_{12} = 0$, $t_1 \neq 0$. (c) Phase III: $t_1 = t_2 = 0$, $t_{12} \neq 0$. (d) Phase IV: $t_1 \neq t_2 \neq t_{12} \neq 0$. The colors indicate the S_z character of each band, and for phases I and II, only the energy states corresponding to the $S_z = \uparrow$ sector are shown.

[1] B. Dieny, I. L. Prejbeanu, K. Garello, P. Gambardella, P. Freitas, R. Lehndorff, W. Raberg, U. Ebels, S. O. Demokritov, J. Akerman *et al.*, Opportunities and challenges for spintronics in the microelectronics industry, Nat. Electron. **3**, 446 (2020).

[2] J. F. Sierra, J. Fabian, R. K. Kawakami, S. Roche, and S. O. Valenzuela, Van der Waals heterostructures for spintronics and opto-spintronics, Nat. Nanotechnol. **16**, 856 (2021).

[3] H. Yang, S. O. Valenzuela, M. Chshiev, S. Couet, B. Dieny, B. Dlubak, A. Fert, K. Garello, M. Jamet, D.-E. Jeong, K. Lee, T. Lee, M.-B. Martin, G. S. Kar, P. Sénéor, H.-J. Shin, and S. Roche, Two-dimensional materials prospects for non-volatile spintronic memories, Nature (London) **606**, 663 (2022).

[4] H. Kontani, T. Tanaka, D. S. Hirashima, K. Yamada, and J. Inoue, Giant intrinsic spin and orbital Hall effects in Sr$_2$MO$_4$ (M = Ru, Rh, Mo), Phys. Rev. Lett. **100**, 096601 (2008).

[5] D. Go, D. Jo, C. Kim, and H.-W. Lee, Intrinsic spin and orbital Hall effects from orbital texture, Phys. Rev. Lett. **121**, 086602 (2018).

[6] L. Salemi and P. M. Oppeneer, First-principles theory of intrinsic spin and orbital Hall and nernst effects in metallic monoatomic crystals, Phys. Rev. Mater. **6**, 095001 (2022).

[7] I. Baek and H.-W. Lee, Negative intrinsic orbital Hall effect in group XIV materials, Phys. Rev. B **104**, 245204 (2021).

[8] H. Lee, B. Choi, and H.-W. Lee, Orientational dependence of intrinsic orbital and spin Hall effects in hcp structure materials, Phys. Rev. B **105**, 035142 (2022).

[9] G. Sala and P. Gambardella, Giant orbital Hall effect and orbital-to-spin conversion in 3d, 5d, and 4f metallic heterostructures, Phys. Rev. Res. **4**, 033037 (2022).

[10] D. B. Fonseca, L. L. A. Pereira, and A. L. R. Barbosa, Orbital Hall effect in mesoscopic devices, Phys. Rev. B **108**, 245105 (2023).

[11] S. Bhowal and G. Vignale, Orbital Hall effect as an alternative to valley Hall effect in gapped graphene, Phys. Rev. B **103**, 195309 (2021).

[12] A. Pezo, D. G. Ovalle, and A. Manchon, Orbital Hall effect in crystals: Interatomic versus intra-atomic contributions, Phys. Rev. B **106**, 104414 (2022).

[13] A. Pezo, D. García Ovalle, and A. Manchon, Orbital Hall physics in two-dimensional Dirac materials, Phys. Rev. B **108**, 075427 (2023).

[14] O. Busch, I. Mertig, and B. Göbel, Orbital Hall effect and orbital edge states caused by s electrons, Phys. Rev. Res. **5**, 043052 (2023).

[15] J.-H. Park, C. H. Kim, J.-W. Rhim, and J. H. Han, Orbital Rashba effect and its detection by circular dichroism angle-resolved photoemission spectroscopy, Phys. Rev. B **85**, 195401 (2012).

[16] A. Johansson, B. Göbel, J. Henk, M. Bibes, and I. Mertig, Spin and orbital Edelstein effects in a two-dimensional electron gas: Theory and application to SrTiO$_3$ interfaces, Phys. Rev. Res. **3**, 013275 (2021).

[17] S. Ding, Z. Liang, D. Go, C. Yun, M. Xue, Z. Liu, S. Becker, W. Yang, H. Du, C. Wang, Y. Yang, G. Jakob, M. Kläui, Y. Mokrousov, and J. Yang, Observation of the orbital Rashba-Edelstein magnetoresistance, Phys. Rev. Lett. **128**, 067201 (2022).

[18] A. E. Hamdi, J.-Y. Chauleau, M. Boselli, C. Thibault, C. Gorini, A. Smogunov, C. Barreteau, S. Gariglio, J.-M. Triscone, and M. Viret, Observation of the orbital inverse Rashba–Edelstein effect, Nat. Phys. **19**, 1855 (2023).

[19] T. G. Rappoport, First light on orbitronics as a viable alternative to electronics, Nature (London) **619**, 38 (2023).

[20] B. A. Bernevig, T. L. Hughes, and S.-C. Zhang, Orbitronics: The intrinsic orbital current in *p*-doped silicon, Phys. Rev. Lett. **95**, 066601 (2005).

[21] D. Go, D. Jo, H.-W. Lee, M. Kläui, and Y. Mokrousov, Orbitronics: Orbital currents in solids, Europhys. Lett. **135**, 37001 (2021).

[22] Y.-G. Choi, D. Jo, K.-H. Ko, D. Go, K.-H. Kim, H. G. Park, C. Kim, B.-C. Min, G.-M. Choi, and H.-W. Lee, Observation of the orbital Hall effect in a light metal Ti, Nature (London) **619**, 52 (2023).

[23] I. Lyalin, S. Alikhah, M. Berritta, P. M. Oppeneer, and R. K. Kawakami, Magneto-optical detection of the orbital Hall effect in chromium, Phys. Rev. Lett. **131**, 156702 (2023).

[24] H. Hayashi, D. Jo, D. Go, T. Gao, S. Haku, Y. Mokrousov, H.-W. Lee, and K. Ando, Observation of long-range orbital transport and giant orbital torque, Commun. Phys. **6**, 32 (2023).

[25] T. S. Seifert, D. Go, H. Hayashi, R. Rouzegar, F. Freimuth, K. Ando, Y. Mokrousov, and T. Kampfrath, Time-domain observation of ballistic orbital-angular-momentum currents with giant relaxation length in tungsten, Nat. Nanotechnol. **18**, 1132 (2023).

[26] D. Go and H.-W. Lee, Orbital torque: Torque generation by orbital current injection, Phys. Rev. Res. **2**, 013177 (2020).

[27] S. Ding, A. Ross, D. Go, L. Baldrati, Z. Ren, F. Freimuth, S. Becker, F. Kammerbauer, J. Yang, G. Jakob, Y. Mokrousov, and M. Kläui, Harnessing orbital-to-spin conversion of interfacial orbital currents for efficient spin-orbit torques, Phys. Rev. Lett. **125**, 177201 (2020).

[28] D. Lee, D. Go, H.-J. Park, W. Jeong, H.-W. Ko, D. Yun, D. Jo, S. Lee, G. Go, J. H. Oh, K.-J. Kim, B.-G. Park, B.-C. Min, H. C. Koo, H.-W. Lee, O. Lee, and K.-J. Lee, Orbital torque in magnetic bilayers, Nat. Commun. **12**, 6710 (2021).

[29] R. Fukunaga, S. Haku, H. Hayashi, and K. Ando, Orbital torque originating from orbital Hall effect in Zr, Phys. Rev. Res. **5**, 023054 (2023).

[30] D. Go, K. Ando, A. Pezo, S. Blügel, A. Manchon, and Y. Mokrousov, Orbital pumping by magnetization dynamics in ferromagnets, arXiv:2309.14817

[31] H. Hayashi, D. Go, S. Haku, Y. Mokrousov, and K. Ando, Observation of orbital pumping, Nat. Electron (2024), doi: 10.1038/s41928-024-01193-1.

[32] L. M. Canonico, T. P. Cysne, T. G. Rappoport, and R. B. Muniz, Two-dimensional orbital Hall insulators, Phys. Rev. B **101**, 075429 (2020).

[33] L. M. Canonico, T. P. Cysne, A. Molina-Sanchez, R. B. Muniz, and T. G. Rappoport, Orbital Hall insulating phase in transition metal dichalcogenide monolayers, Phys. Rev. B **101**, 161409(R) (2020).

[34] S. Bhowal and S. Satpathy, Intrinsic orbital and spin Hall effects in monolayer transition metal dichalcogenides, Phys. Rev. B **102**, 035409 (2020).

[35] T. P. Cysne, M. Costa, L. M. Canonico, M. B. Nardelli, R. B. Muniz, and T. G. Rappoport, Disentangling orbital and valley Hall effects in bilayers of transition metal dichalcogenides, Phys. Rev. Lett. **126**, 056601 (2021).

[36] T. P. Cysne, S. Bhowal, G. Vignale, and T. G. Rappoport, Orbital Hall effect in bilayer transition metal dichalcogenides:

From the intra-atomic approximation to the Bloch states orbital magnetic moment approach, Phys. Rev. B **105**, 195421 (2022).

[37] E. Ridolfi, L. R. F. Lima, E. R. Mucciolo, and C. H. Lewenkopf, Electronic transport in disordered MoS_2 nanoribbons, Phys. Rev. B **95**, 035430 (2017).

[38] H. Rostami, R. Asgari, and F. Guinea, Edge modes in zigzag and armchair ribbons of monolayer MoS_2, J. Phys.: Condens. Matter **28**, 495001 (2016).

[39] M. Costa, B. Focassio, L. M. Canonico, T. P. Cysne, G. R. Schleder, R. B. Muniz, A. Fazzio, and T. G. Rappoport, Connecting higher-order topology with the orbital Hall effect in monolayers of transition metal dichalcogenides, Phys. Rev. Lett. **130**, 116204 (2023).

[40] W. A. Benalcazar, T. Li, and T. L. Hughes, Quantization of fractional corner charge in C_n-symmetric higher-order topological crystalline insulators, Phys. Rev. B **99**, 245151 (2019).

[41] J. Zeng, H. Liu, H. Jiang, Q.-F. Sun, and X. C. Xie, Multiorbital model reveals a second-order topological insulator in $1H$ transition metal dichalcogenides, Phys. Rev. B **104**, L161108 (2021).

[42] S. Qian, G.-B. Liu, C.-C. Liu, and Y. Yao, C_n-symmetric higher-order topological crystalline insulators in atomically thin transition metal dichalcogenides, Phys. Rev. B **105**, 045417 (2022).

[43] S. Han, H.-W. Lee, and K.-W. Kim, Orbital dynamics in centrosymmetric systems, Phys. Rev. Lett. **128**, 176601 (2022).

[44] S. Han, H.-W. Lee, and K.-W. Kim, Microscopic study of orbital textures, Curr. Appl. Phys. **50**, 13 (2023).

[45] P. Eck, Y. Fang, D. Di Sante, G. Sangiovanni, and J. Cano, Recipe for higher order topology on the triangular lattice, Phys. Rev. B **107**, 115130 (2023).

[46] G.-B. Liu, W.-Y. Shan, Y. Yao, W. Yao, and D. Xiao, Three-band tight-binding model for monolayers of group-VIB transition metal dichalcogenides, Phys. Rev. B **88**, 085433 (2013).

[47] A. Bastin, C. Lewiner, O. Betbeder-Matibet, and P. Nozieres, Quantum oscillations of the Hall effect of a fermion gas with random impurity scattering, J. Phys. Chem. Solids **32**, 1811 (1971).

[48] J. H. García, L. Covaci, and T. G. Rappoport, Real-space calculation of the conductivity tensor for disordered topological matter, Phys. Rev. Lett. **114**, 116602 (2015).

[49] J. H. Garcia and T. G. Rappoport, Kubo–Bastin approach for the spin Hall conductivity of decorated graphene, 2D Mater. **3**, 024007 (2016).

[50] S. M. João, M. Anđelković, L. Covaci, T. G. Rappoport, J. M. V. P. Lopes, and A. Ferreira, KITE: High-performance accurate modelling of electronic structure and response functions of large molecules, disordered crystals and heterostructures, R. Soc. Open Sci. **7**, 191809 (2020).

[51] Z. Fan, J. H. Garcia, A. W. Cummings, J. E. Barrios-Vargas, M. Panhans, A. Harju, F. Ortmann, and S. Roche, Linear scaling quantum transport methodologies, Phys. Rep. **903**, 1 (2021).

[52] LSQUANT, https://www.lsquant.org.

[53] T. P. Cysne, F. S. M. Guimarães, L. M. Canonico, T. G. Rappoport, and R. B. Muniz, Orbital magnetoelectric effect in zigzag nanoribbons of *p*-band systems, Phys. Rev. B **104**, 165403 (2021).

[54] C. L. Kane and E. J. Mele, Z_2 topological order and the quantum spin Hall effect, Phys. Rev. Lett. **95**, 146802 (2005).

[55] Z. Song, Z. Fang, and C. Fang, $(d - 2)$-dimensional edge states of rotation symmetry protected topological states, Phys. Rev. Lett. **119**, 246402 (2017).

[56] W. A. Benalcazar, B. A. Bernevig, and T. L. Hughes, Electric multipole moments, topological multipole moment pumping, and chiral hinge states in crystalline insulators, Phys. Rev. B **96**, 245115 (2017).

[57] J. Kruthoff, J. de Boer, J. van Wezel, C. L. Kane, and R.-J. Slager, Topological classification of crystalline insulators through band structure combinatorics, Phys. Rev. X **7**, 041069 (2017).

[58] B. K. Nikolić, L. P. Zârbo, and S. Souma, Mesoscopic spin Hall effect in multiprobe ballistic spin-orbit-coupled semiconductor bridges, Phys. Rev. B **72**, 075361 (2005).

[59] B. K. Nikolić and L. P. Zârbo, Extrinsically vs. intrinsically driven spin Hall effect in disordered mesoscopic multiterminal bars, Europhys. Lett. **77**, 47004 (2007).

[60] J. H. Bardarson, İ Adagideli, and P. Jacquod, Mesoscopic spin Hall effect, Phys. Rev. Lett. **98**, 196601 (2007).

[61] C. W. Groth, M. Wimmer, A. R. Akhmerov, and X. Waintal, Kwant: A software package for quantum transport, New J. Phys. **16**, 063065 (2014).